Article

X-ray CT metal artifact reduction using wavelet domain L0 sparse regularization

MEHRANIAN, Abolfazl, *et al*.

Abstract

X-ray computed tomography (CT) imaging of patients with metallic implants usually suffers from streaking metal artifacts. In this paper, we propose a new projection completion metal artifact reduction (MAR) algorithm by formulating the completion of missing projections as a regularized inverse problem in the wavelet domain. The Douglas-Rachford splitting (DRS) algorithm was used to iteratively solve the problem. Two types of prior information were exploited in the algorithm: 1) the sparsity of the wavelet coefficients of CT sinograms in a dictionary of translation-invariant wavelets and 2) the detail wavelet coefficients of a prior sinogram obtained from the forward projection of a segmented CT image. A pseudo- L0 synthesis prior was utilized to exploit and promote the sparsity of wavelet coefficients. The proposed L0-DRS MAR algorithm was compared with standard linear interpolation and the normalized metal artifact reduction (NMAR) approach proposed by Meyer using both simulated and clinical studies including hip prostheses, dental fillings, spine fixation and electroencephalogram electrodes in brain imaging. The [...]

Reference

MEHRANIAN, Abolfazl, *et al*. X-ray CT metal artifact reduction using wavelet domain L0 sparse regularization. *IEEE Transactions on Medical Imaging*, 2013, vol. 32, no. 9, p. 1707-22

DOI : 10.1109/TMI.2013.2265136
PMID : 23744669

X-ray CT Metal Artifact Reduction Using Wavelet Domain L_0 Sparse Regularization

Abolfazl Mehranian, Mohammad Reza Ay, *Member, IEEE*, Arman Rahmim, *Senior Member, IEEE*, and Habib Zaidi*, *Senior Member, IEEE*

***Abstract*—X-ray computed tomography (CT) imaging of patients with metallic implants usually suffers from streaking metal artifacts. In this paper, we propose a new projection completion metal artifact reduction (MAR) algorithm by formulating the completion of missing projections as a regularized inverse problem in the wavelet domain. The Douglas–Rachford splitting (DRS) algorithm was used to iteratively solve the problem. Two types of prior information were exploited in the algorithm: 1) the sparsity of the wavelet coefficients of CT sinograms in a dictionary of translation-invariant wavelets and 2) the detail wavelet coefficients of a prior sinogram obtained from the forward projection of a segmented CT image. A pseudo-L_0 synthesis prior was utilized to exploit and promote the sparsity of wavelet coefficients. The proposed L_0-DRS MAR algorithm was compared with standard linear interpolation and the normalized metal artifact reduction (NMAR) approach proposed by Meyer *et al.* using both simulated and clinical studies including hip prostheses, dental fillings, spine fixation and electroencephalogram electrodes in brain imaging. The qualitative and quantitative evaluations showed that our algorithm substantially suppresses streaking artifacts and can outperform both linear interpolation and NMAR algorithms.**

***Index Terms*—Metal artifact reduction (MAR), streaking artifacts, wavelets, X-ray computed tomography (CT), L_0 sparse regularization.**

I. Introduction

THE NONLINEAR absorption of polychromatic X-ray beams used in X-ray computed tomography (CT) often results in beam hardening and the selective absorption of X-ray photons [1]. In the presence of strongly attenuating objects such as metallic implants, beam hardening and scattering is usually so strong that the detectors sensing the implants experience severe photon starvation and thus the relevant log-processed projection data become corrupted and inconsistent [2], [3]. Consequently, the data inconsistency appears as dark and bright streaking artifacts during image reconstruction, which can obscure crucial diagnostic information in tissues surrounding the implants [4]–[6]. Moreover, as shown in [7], nonlinear partial volume effects and noise can also give rise to data corruption and hence streaking artifacts. Over the years, the prevalence of CT imaging in clinical practice and the need for improved image quality in patients bearing metallic implants have spurred continuous efforts towards the development of metal artifact reduction (MAR) algorithms to compensate for corrupted and missing projections, thus mitigating metal artifacts. MAR algorithms fall into two classes: projection completion and iterative image reconstruction algorithms.

In the projection completion approach, which is often followed by filtered-back-projection (FBP) image reconstruction, the missing projections are synthesized from neighboring projections using linear and polynomial interpolation [4], [8]–[10], wavelet interpolation [11], adaptive filtering [12], [13], and inpainting [14]–[17] techniques. Other approaches aim at replacing the missing projections with those available in opposite view angles or adjacent CT slices [18]–[20] or the projections obtained from forward projection of tissue-segmented CT images [21]–[24]. The efficiency of these algorithms in the recovery of missing projections hinges on how robustly they can exploit the available projection data or utilize *a priori* information about missing projections. In fact, if not appropriately developed, these methods might induce new artifacts. Recently, Meyer *et al.* [25] proposed a very promising projection-based normalized MAR (NMAR) algorithm to facilitate the interpolation of missing projections without introducing new severe artifacts. In this algorithm, the original sinogram is first normalized by a sinogram obtained from a tissue-segmented CT image, called *prior* image, and then the missing data are linearly interpolated. Finally, the resulting sinogram is denormalized. In general, projection completion algorithms should be preceded by a metal trace identification step, in which projections running through metallic implants (i.e., corrupted or missing projections) are identified. This is achieved by either 1) segmentation of CT images for metallic implants and forward projection of the resulting *metal-only* image into an artificial sinogram domain [4], [26], [27], or 2) direct segmentation of raw sinogram data for corrupted projections [10], [13], [16].

Manuscript received January 14, 2013; revised May 03, 2013; accepted May 22, 2013. Date of publication June 03, 2013; date of current version August 28, 2013. This work was supported in part by the Swiss National Science Foundation under Grant SNSF 31003A-135576, in part by the Indo-Swiss Joint Research Programme ISJRP 138866, and in part by the Geneva University Hospital under Grant PRD 11-II-1. *Asterisk indicates corresponding author.*

A. Mehranian is with Division of Nuclear Medicine and Molecular Imaging, Geneva University Hospital, CH-1211 Geneva, Switzerland (e-mail: mehrani1@etu.unige.ch).

M. R. Ay is with the Department of Medical Physics and Biomedical Engineering, and Research Center for Molecular and Cellular Imaging, Tehran University of Medical Sciences, Tehran, Iran (e-mail: mohammadreza_ay@sina.tums.ac.ir).

A. Rahmim is with the Department of Radiology, School of Medicine, and Department of Electrical and Computer Engineering, Johns Hopkins University, Baltimore, MD 21287 USA (e-mail: arahmim1@jhmi.edu).

*H. Zaidi is with the Division of Nuclear Medicine and Molecular Imaging, Geneva University Hospital, CH-1211 Geneva, Switzerland, Geneva Neuroscience Center, Geneva University, CH-1211 Geneva, Switzerland, and also with the Department of Nuclear Medicine and Molecular Imaging, University of Groningen, University Medical Center Groningen, 9700 RB Groningen, The Netherlands (e-mail: habib.zaidi@hcuge.ch).

Digital Object Identifier 10.1109/TMI.2013.2265136

During the last decade, iterative model-based image reconstruction methods have established another class of algorithms: these techniques originate from statistical methods that estimate missing or incomplete data [28]. They can be easily adapted to truncated and missing sinogram data by ignoring or reducing statistical contributions of corrupted projections, and by imposing constraints and prior knowledge on the images being reconstructed [27], [29]–[31]. In this class of algorithms, the missing projections are identified by either image- and sinogram-based approaches used in projection completion [29], [32] or a hybrid of both involving iterative metal-only image reconstruction and metal-trace segmentation [27], [33], [34]. These algorithms, however, cannot entirely compensate for severe data corruptions [35], and hence, their initiation and combination with projection completion algorithms have also been investigated [32], [36]. Compared to projection completion methods, model-based iterative image reconstruction is computationally intensive. Recently, Van Slambrouck *et al.* [37] proposed a region-based iterative reconstruction method to reduce the computational complexity of this class of MAR algorithms. In this method, the regions containing metals are reconstructed using a fully polychromatic spectral model, while other regions are reconstructed using a simpler model that only considers the spectral behavior of water attenuation. Although this approach tends to preserve structures near metallic implants, the reconstructed images still suffer from streaking artifacts in comparison with linear interpolation and Meyer's NMAR approaches.

In this work, we propose a new projection completion MAR algorithm in which the recovery of missing projections is formulated as a regularized inverse problem and some prior information about the underlying complete sinogram is exploited during the optimization process. Specifically, we propose a sparse synthesis regularization for the estimation of missing projections in the wavelet domain and exploit two types of prior information: 1) the sparsity of a CT sinogram in a dictionary of translation-invariant wavelets and 2) the detail wavelet coefficients of a prior sinogram obtained by a tissue-segmented CT image. The Doglous–Rachford Splitting (DRS) algorithm was used for the optimization of the problem. The sparsity of sinograms in the wavelet domain is promoted by a pseudo L_0 norm based on the homotopic approximation of an L_0 norm. We also compare the performance of the proposed MAR algorithm with standard linear interpolation and NMAR algorithms using simulation and clinical studies to assess its potential and demonstrate its outperformance over these MAR approaches.

II. Materials and Methods

A. Problem Formulation

We denote the 2-D log-processed sinogram of a CT slice as a vector in $\mathbb{R}_+^N$, where N is the number of detector channels times the number of projection angles. Let $\boldsymbol{f}$ be an observed sinogram with metal traces that corrupt the projection data at the locations indexed by the set $\boldsymbol{\Omega} \subset \{1, \ldots, N\}$. In the recovery of missing projections, we formulate the following forward model:

$$\boldsymbol{y} = \boldsymbol{\Phi f} + \boldsymbol{n} \tag{1}$$

where $\boldsymbol{y} \in \mathbb{R}^M, M < N$, is an incomplete sinogram, $\boldsymbol{\Phi} \in \mathbb{R}^{M \times N}$ is a lossy matrix that removes the projections of $\boldsymbol{f}$ over the set $\boldsymbol{\Omega}$ and $\boldsymbol{n}$ represents data perturbations due to white Gaussian noise (with variance of σ^2). The matrix $\boldsymbol{\Phi}$ can be thought of as an $N \times N$ identity matrix that has been downsized along $r = N - M$ rows, indexed by the set $\boldsymbol{\Omega}$. To estimate a sinogram with complete data, one approach is to invert the problem (1) by minimizing the cost function $(1)/(2\sigma^2)\sum_{i=1}^{M} (y_i - [\boldsymbol{\Phi f}]_i)^2$, which is derived by considering Gaussian noise. However, this minimization has an infinite number of possible solutions. To regulate the solution space and penalize unsatisfactory solutions, one can impose *a priori* knowledge about the solution through a *regularizer* or *prior* $R(\boldsymbol{f})$. Therefore, the solution can be obtained by the following optimization problem:

$$\hat{\boldsymbol{f}} = \underset{\boldsymbol{f} \in \mathbb{R}_+^N}{\operatorname{argmin}} \left\{ \frac{1}{2\sigma^2} \|\boldsymbol{y} - \boldsymbol{\Phi f}\|^2 + \lambda R(\boldsymbol{f}) \right\} \tag{2}$$

where $\|\boldsymbol{x}\|$ stands for the Euclidean (L_2) norm of the vector $\boldsymbol{x}$, which is a special case $(p = 2)$ of the L_p norm defined as $\|\boldsymbol{x}\|_p = (\sum_{i=1} |x_i|^p)^{1/p}$, and λ is a regularization parameter that controls the balance between the fidelity of the solution to the observations and its regularity to prior knowledge.

In the context of compressed sensing and sparse signal recovery, the prior knowledge that an expected signal or solution is sparse (i.e., having many zero components) is exploited to recover it from its samples or incomplete measurements. When $\boldsymbol{f}$ is not sparse directly (e.g., in the sinogram domain), it is possible to explore its sparsity or compressibility in an appropriate sparse representation dictionary [38]. By definition, if $\boldsymbol{f}$ is sparse (or compressible) in the dictionary $\boldsymbol{W} = [w_1, \ldots, w_N]^T \in \mathbb{R}^{N \times K}$, most of its energy is represented by and compressed in a few large magnitude coefficients. In other words, when $\boldsymbol{f}$ is expressed as a linear combination of $K \geq N$ elementary functions, $\boldsymbol{f} = \boldsymbol{W\theta} = \sum_{i=1}^{K} w_i \theta_i$, the majority of the decomposition coefficients, θ_i, are (close to) zero. The dictionary $\boldsymbol{W}$, namely *synthesis* (or reconstruction) operator, often consists of $K = N$ concatenated orthonormal bases or $K > N$ tight frames. In the case of a basis, $\boldsymbol{W}$ is a square full-rank matrix that satisfies, $\boldsymbol{WW}^* = \boldsymbol{W}^*\boldsymbol{W} = \boldsymbol{I}$ where $\boldsymbol{W}^*$ is its conjugate transpose, namely an *analysis* (or decomposition) operator and $\boldsymbol{I}$ is the identity matrix. In the case of a tight frame, $\boldsymbol{W}$ is a nonsquare matrix and a redundant dictionary that only satisfies $\boldsymbol{WW}^* = \boldsymbol{I}$ while $\boldsymbol{W}^*\boldsymbol{W} \neq \boldsymbol{I}$ [39], [40]. Given an appropriate sparse dictionary, the solution of the problem (2) can be alternatively obtained through synthesization from its representation coefficients, i.e., $\hat{\boldsymbol{f}} = \boldsymbol{W}\hat{\boldsymbol{\theta}}$, where

$$\begin{aligned} \hat{\boldsymbol{\theta}} &= \underset{\boldsymbol{\theta} \in \Theta}{\operatorname{argmin}} \left\{ \frac{1}{2\sigma^2} \|\boldsymbol{y} - \boldsymbol{\Phi W\theta}\|^2 + \lambda R(\boldsymbol{\theta}) \right\} \\ \boldsymbol{\Theta} &= \left\{ \boldsymbol{\theta} \,|\, \boldsymbol{\theta} \in \mathbb{R}^K, \boldsymbol{W\theta} \in \mathbb{R}_+^N \right\}. \end{aligned} \tag{3}$$

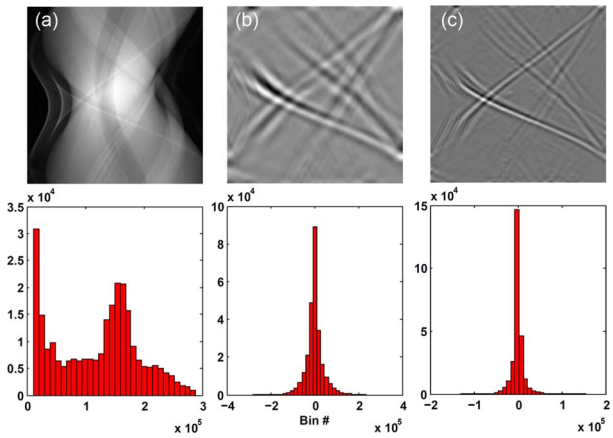

Fig. 1. Top: (a) A 512 × 512 block of a typical CT sinogram and (b), (c) its two representative detail wavelet coefficients at two different resolution levels. Bottom: The histograms of the images in (a)–(c) over 30 bins.

This formulation is referred to as a synthesis approach, whereas the formulation of the problem (2) with the prior $R(\boldsymbol{W}^*\boldsymbol{f})$ is called an analysis approach [41]. Unless the dictionary is a basis, the two formulations do not result in the same solution. In fact, the synthesis approach emphasizes more on the sparsity of the solution, while the analysis approach emphasizes a balance between the sparsity of decomposition coefficients and the smoothness of the solution [40]. In this study, we made use of a tight frame of translation-invariant wavelets and followed the synthesis approach for the completion of missing projections. We employed Daubechies 7/9 biorthogonal (D7/9) wavelets with four resolution levels and implemented by undecimated discrete wavelet transforms and a lifting scheme. It is worth mentioning that these wavelets are used in the JPEG-2000 image compression standard [42]. Fig. 1 shows a 512 × 512 block of a typical CT sinogram and its two representative detail wavelet coefficients at two different resolution levels.

As seen in histograms, a CT sinogram is not directly sparse, but can have a sparse representation in wavelet domain. One of the most successful priors in describing the usually heavy-tailed density of wavelet coefficients is the generalized Gaussian distribution [43], whose logarithm is the pth power of an L_p norm for $0 < p \leq 2$

$$R(\boldsymbol{\theta}) = \sum_{i=1} |\theta_i|^p = \|\boldsymbol{\theta}\|_p^p. \tag{4}$$

The L_p norm can be utilized to promote the sparsity of the wavelet coefficients. An ideal sparsity-promoting prior is the L_0 norm, $\|\boldsymbol{x}\|_0$, which counts the number of nonzero components of $\boldsymbol{x}$. However, this nonconvex prior results in an intractable optimization problem and require global search optimization techniques such as simulated annealing. There exist convex L_p norms or priors for $p \geq 1$, among which the L_1 norm favors the highest degree of sparsity and hence as a proxy to L_0 norm has garnered significant attention in compressed sensing and sparsity regularization [44]–[46]. The L_0 norm can, however, be homotopically approximated by a pseudo L_0 norm as follows:

$$R(\boldsymbol{\theta}) \lim_{\rho \to 0} = \sum_{i=1} \psi(\theta_i, \rho) \tag{5}$$

where ψ is a quasi-convex potential function with a homotopic parameter ρ. As ρ approaches zero, the pseudo L_0 norm approaches the L_0 norm. In this study, we employed the following log potential function [46], [47]:

$$\pi(\theta, \rho) = \nu \ln\left(1 + \frac{|\theta|}{\rho}\right), \quad \nu = \frac{1}{\ln\left(1 + \frac{1}{\rho}\right)} \tag{6}$$

where ν is a normalization factor. As shown in Fig. 2(a), for large values of ρ, this potential function approaches an absolute value function (associated with L_1 norm) and becomes convex, while for small values of ρ it becomes nonconvex and approaches a zero-one potential function (associated with L_0 norm).

B. Optimization Algorithm

To solve the optimization problem in (3), we follow the Douglas–Rachford splitting (DRS) algorithm, which is targeted for solving the following general minimization problem [48]:

$$\min_{\boldsymbol{\theta} \in \mathcal{H}} \{F_1(\boldsymbol{\theta}) + F_2(\boldsymbol{\theta})\} \tag{7}$$

where F_1 and F_2 are proper, convex and lower semi-continuous (l.s.c) functions in a Hilbert space $\mathcal{H}$. To describe the DRS algorithm, we first need to define the proximity operator $\text{prox}_F(\cdot)$ of a proper, convex and l.s.c function F that maps $\mathcal{H}$ to $\mathbb{R}$.

For every $\boldsymbol{z} \in \mathcal{H}$, the minimum energy of the envelope of F is achieved at a unique point, $\text{prox}_F(\boldsymbol{\theta})$, called proximal map or proximum, i.e., ([49])

$$\text{prox}_F(\boldsymbol{\theta}) = \underset{\boldsymbol{z} \in \mathcal{H}}{\text{argmin}} \left\{ \frac{1}{2}\|\boldsymbol{z} - \boldsymbol{\theta}\|^2 + F(\boldsymbol{z}) \right\}. \tag{8}$$

By this definition, the DRS algorithm iteratively estimates the minimizer $\hat{\boldsymbol{\theta}}$ of the problem (7) as follows:

$$\hat{\boldsymbol{\theta}}^k = \text{prox}_{F_1}(\boldsymbol{\theta}^k) + a^k, \tag{9}$$

$$\boldsymbol{\theta}^{k+1} = \boldsymbol{\theta}^k + \gamma^k(\text{prox}_{F_2}(2\hat{\boldsymbol{\theta}}^k - \boldsymbol{\theta}^k) - \hat{\boldsymbol{\theta}}^k + b^k) \tag{10}$$

where $\text{prox}_{F_1}(\cdot)$ and $\text{prox}_{F_2}(\cdot)$ are the proximity operators of the functions F_1 and F_2, γ^k is a (variable) relaxation parameter in the range (0, 2) and a^k and b^k are two sequences associated with the proximity operators allowing for approximations in their calculation and inexact implementation. The existence and uniqueness conditions of a solution to the optimization problem (7) using the DRS algorithm are discussed in [48].

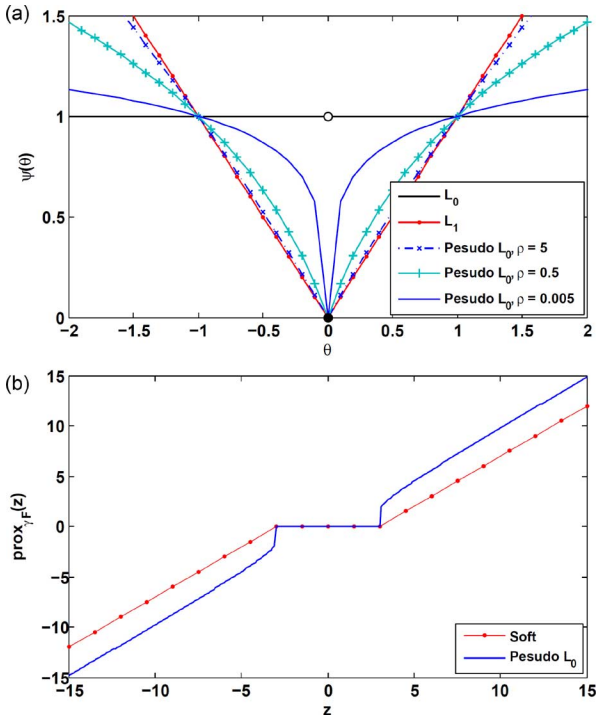

Fig. 2. (a) Comparison of the potential functions of $\boldsymbol{L_1}$, pseudo $\boldsymbol{L_0}$ and $\boldsymbol{L_0}$ norms. (b) Thresholding rules induced by $\boldsymbol{L_1}$ and pseudo $\boldsymbol{L_0}$ norms.

For theoretical discussions on the convergence of the DRS algorithm for nonconvex problems, interested readers should consult [50]. To apply the DRS to the problem (3), we need to obtain the proximity operator of the data fidelity term $D(\boldsymbol{\theta}) = (1)/(2\sigma^2)\|\boldsymbol{y} - \boldsymbol{\Phi W\theta}\|^2$, (i.e., F_1) and the operator of the prior $R(\boldsymbol{\theta})$ for a pseudo L_0 norm (i.e., F_2). In the following subsections, we derive closed-form solutions for these operators and also discuss the incorporation of prior wavelet coefficients into the DRS algorithm. As we obtain closed-form solution for the proximity maps, we can simply set the a^k and b^k terms to zero in (9) and (10).

1) The Proximal Map of Data Fidelity: The proximal map of the data fidelity term, i.e.,

$$\text{prox}_{\sigma D}(\boldsymbol{\theta}) = \underset{\boldsymbol{z}\in\mathbb{R}^K}{\text{argmin}} \left\{ \frac{1}{2}\|\boldsymbol{z}-\boldsymbol{\theta}\|^2 + \frac{1}{2\sigma^2}\|\boldsymbol{y}-\boldsymbol{\Phi W z}\|^2 \right\} \tag{11}$$

is obtained by equating the derivative of its objective to zero, thereby the solution is given by: $\hat{\boldsymbol{z}} = (\boldsymbol{W}^*\boldsymbol{\Phi}^T\boldsymbol{\Phi W} + \sigma^2\boldsymbol{I})^{-1}(\sigma^2\boldsymbol{\theta} + \boldsymbol{W}^*\boldsymbol{\Phi}^T\boldsymbol{y})$. To calculate the inverse term in this equation, we follow the matrix inversion lemma and make use of the fact that $\boldsymbol{\Phi\Phi}^T = \boldsymbol{WW}^* = \boldsymbol{I}$, thereby the proximal mapping is given by

$$\text{prox}_{\sigma D}(\boldsymbol{\theta}) = \boldsymbol{\theta} + \frac{1}{1+\sigma^2}\boldsymbol{W}^*\boldsymbol{\Phi}^T(\boldsymbol{y} - \boldsymbol{\Phi W\theta}). \tag{12}$$

In this study, we consider that the operator $\boldsymbol{\Phi}$ in (1) removes the projections of $\boldsymbol{f}$ without introducing noise. As a result, the variance of noise, σ^2, in (12) is set to zero.

2) The Proximal Map of the Prior: The pseudo L_0 norm defined in (5) is separable and follows the form $R(\boldsymbol{z}) = \sum_i \psi(z_i)$, where $\psi(z) = \nu \ln(1 + (|z|)/(\rho))$. The proximal map of such a separable function can therefore be obtained separately with respect to each component as follows:

$$\text{prox}_{\lambda\psi}(\theta_i) = \underset{\boldsymbol{z}_i\in\mathbb{R}}{\text{argmin}} \left\{ \frac{1}{2}(z_i-\theta_i)^2 + \lambda\psi(z_i) \right\}. \tag{13}$$

One can obtain a closed-form solution to the above problem by the following thresholding rule (see Appendix A for more details):

$$\text{prox}_{\lambda\psi}(\theta_i) = \begin{cases} \frac{1}{2}(\theta_i - \rho + \sqrt{(\theta_i+\rho)^2 - 4\lambda\nu}), & \theta_i > T \\ 0, & |\theta_i| \le T \\ \frac{1}{2}(\theta_i + \rho - \sqrt{(\theta_i-\rho)^2 - 4\lambda\nu}), & \theta_i < -T \end{cases} \tag{14}$$

where $T = 2\sqrt{\lambda\nu} - \rho$. In this rule, as $\rho \to 0$, the threshold T is slowly decreased. It can therefore play a role similar to the cooling parameter of simulated annealing techniques, allowing the solution to escape from local minima. As shown in Appendix A, when $\rho \to \infty$ the solution of problem (13) is given by a *soft* thresholding rule [51], which is in fact the proximity operator of an L_1 norm. Fig. 2(b) compares the derived thresholding rule with a soft thresholding rule. It can be seen that the pseudo L_0 rule tends to linearly shrink the coefficients θ_i in $|\theta_i| > T$.

3) Incorporation of Prior Wavelet Coefficients: To improve the accuracy of the restored wavelet coefficients and hence the missing sinogram projections, we modify the DRS algorithm in order to incorporate some prior wavelet coefficients obtained from the sinogram of a prior image. For this purpose, we introduce the detail sub-bands of such prior wavelet coefficients, $\boldsymbol{\theta}_p$, into (10) as follows:

$$\boldsymbol{\theta}^k = \boldsymbol{\theta}^{k+1} + \boldsymbol{\gamma}^k \left(prox_{F_2}(2\hat{\boldsymbol{\theta}}^k - \boldsymbol{\theta}^k - \boldsymbol{\theta}_p) - \hat{\boldsymbol{\theta}}^k + \boldsymbol{\theta}_p \right) \tag{15}$$

where $\boldsymbol{\theta}_p$ is in fact the wavelet coefficients with zeroed approximate sub-band. In this modification, the thresholding of wavelet coefficients is disturbed by subtracting the energy corresponding to the prior coefficients, and then removed energy is added back. The rationale behind this modification is based on the observation that the algorithm can properly restore the approximate sub-band of the wavelet coefficients of missing projections from adjacent coefficients. However, as usually a large area of sinogram projections is corrupted by metallic implants, the detail coefficients are not properly restored. Therefore, the introduction of prior detail coefficients can improve the accuracy of the estimation. To this end, Algorithm 1 summarizes the proposed algorithm in the recovery of missing projections.

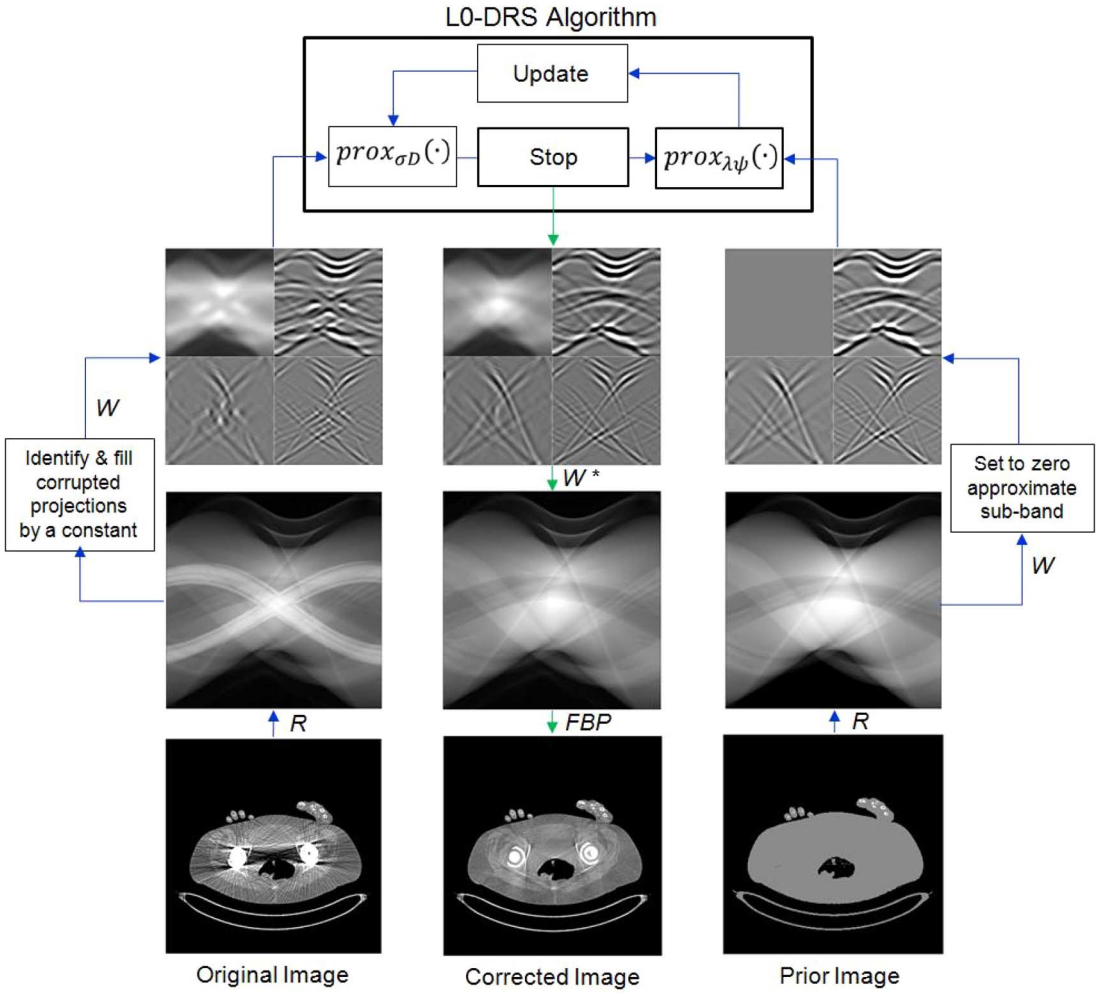

Fig. 3. Flowchart of the proposed wavelet-based L_0-DRS algorithm. In this algorithm, the uncorrected image is segmented to produce metallic implants and a prior image. The images are then forward projected by the operator R. The corrupted projections are identified and filled with a constant value. The resulting sinograms are transformed into the wavelet domain by the operator W. The approximate sub-band of the prior wavelet coefficients is set to zero. The wavelet coefficients are fed into the DRS algorithm, which estimates the wavelet coefficients of missing projections according to Algorithm 1. The estimated coefficients are transformed back into the sinogram domain by the operator W^* and the corrected images are reconstructed using filtered back-projection (FBP) and superimposed by the implants.

ALGORITHM **1: L_0-DRS** ALGORITHM

Choose: $\mu, \gamma^k, \lambda, \eta$ and initialize: $\boldsymbol{\theta}_p, \boldsymbol{\theta}^0 = \boldsymbol{W}^* \boldsymbol{f}^0, \rho^0 = 1, \nu^0 = \ln(1 + 1/\rho^0), k = 0$

While $(\|\boldsymbol{\theta}^{k+1} - \boldsymbol{\theta}^k\|/\|\boldsymbol{\theta}^k\| < \eta)$ **do**,

1. Compute the proximal map, $\hat{\boldsymbol{\theta}}^k$, of data fidelity for $\boldsymbol{\theta}^k$ according to (12).
2. Threshold the coefficients $2\hat{\boldsymbol{\theta}}^k - \boldsymbol{\theta}^k - \boldsymbol{\theta}_p$ according to (14).
3. Compute $\boldsymbol{\theta}^{k+1}$ according to (15).
4. Impose nonnegativity constraint: $\boldsymbol{\theta}^{k+1} = W^*[W\boldsymbol{\theta}^{k+1}]_+$.
5. Update the variables: $\rho^{k+1} = \mu\rho^k, \nu^{k+1} = \ln(1 + 1/\rho^{k+1}), k = k + 1$.

Output: $\hat{\boldsymbol{f}} = \boldsymbol{W}\hat{\boldsymbol{\theta}}^k$.

In this algorithm, we let ρ iteratively approaching zero using the relaxation parameter $0 < \mu < 1$ and set $\gamma^k = 1$. The regularization parameter λ should be large enough to ensure the thresholding of the wavelet coefficients. Therefore, we set it to the maximum projection value of $\boldsymbol{y}$. A global convergence was declared when the normalized L_2 error of two successive iterates falls below a tolerance of $\eta = 1 \times 10^{-3}$. The initial guess of the wavelet coefficient, $\boldsymbol{\theta}^0$, is obtained from the forward wavelet transform of a sinogram, in which missing projections have been filled with a nonzero constant value. Fig. 3 shows the flow chart of the proposed algorithm. The missing projections are identified by the forward projection (or radon transform, R) of a metal only image, obtained from the segmentation of metallic implants in the uncorrected image. The prior image was obtained by the approach proposed by Meyer *et al.* [25] (see next section for details). In this work, we followed a block-wise approach in the recovery of missing projections, using two overlapping 512×512 blocks, automatically portrayed on missing regions of the sinograms (see next section for the specifications of sinograms). This approach favors the fact that discrete wavelet transforms are typically implemented for dyadic- and square-sized matrices.

C. Simulation and Clinical Studies

In this study, the performance of the proposed MAR algorithm was evaluated on artificial sinograms (raw data) obtained from the forward projection of original uncorrected CT images. To acquire such data in conditions closely matched to actual acquisition, we consider the fan-beam geometry of a simulated single-slice CT scanner with 888 detector channels, 984 angular samples over a 360 orbit, detector pitch of 1 mm, 949 mm source to detector distance, 541 mm source to iso-center distance, 408 mm iso-center to detector distance. The geometric system matrix describing this scanner was generated by the MATLAB-based Image Reconstruction Toolbox [52] and line integrals were employed during forward projection to obtain the Radon transform. Following the correction of the sinograms for corrupted projections, the corrected images were reconstructed using the FBP algorithm, with Ram–Lak filter, for a resolution of 512×512, pixel size of 0.97 mm and a 500-mm field-of-view. The Ram–Lak filter was chosen to best preserve the sharpness of the reconstructed images. Algorithm 1 together with undecimated discrete wavelet transforms were implemented in MATLAB 2010a, running on a 12-core workstation with 2.40-GHz Intel Xeon processors and 32 GB memory.

In this study, we followed Meyer's approach [25] to define the prior image. In this approach, the original CT image, contaminated by streaking artifacts is segmented for three tissue types: air, bone, and soft tissue. For this purpose, we used simple thresholding to segment CT images. Soft tissues were segmented using a threshold of 624 HU, while bone tissues were segmented at 1300–1400 HU, depending on the organ or slice being examined. Note that dark and bright streak artifacts can be falsely segmented as air and bone in the segmented soft and bone images, respectively. These false segmentations were respectively eliminated by close and open morphological filtering. As suggested by Prell *et al.* [23], an alternative way in such cases can be the segmentation of an image precorrected using a linear interpolation MAR algorithm. Following the segmentation, the CT numbers of air and soft tissue regions were set to -1000 and 0 HU, respectively, and the numbers of bone regions were kept the same as the original image because of the variation of bone density and CT numbers. In the obtained prior image, we assigned the CT number of soft tissue to metal implants. The performance of the proposed MAR algorithm was evaluated using a number of simulated and clinical studies of patients with hip prostheses, electroencephalogram (EEG) electrodes, dental fillings and spine fixation. As mentioned earlier, the missing projections and thereby the metal trace set $\boldsymbol{\Omega}$, were identified by the forward projection of a segmented metal only image. The segmentation of metallic implants was performed by a simple thresholding at about 3000 HU for dental fillings and 2000 HU for other implants. In some cases, a morphological dilation was performed on the segmented implants to more accurately include all pixels belonging to the implants.

To objectively evaluate the performance of the proposed MAR algorithms with respect to ground truth CT image (i.e., without metal artifacts), we retrospectively generated metal artifacts in the artifact-free CT image of two patients with simulated bilateral hip prostheses and head EEG electrodes (see Fig. 4). To simulate beam hardening and the resulting streaking artifacts, we modeled the polychromatic propagation of X-ray beams through the patient body. For this purpose, the original CT images were segmented into three classes, i.e., air, soft tissue, bone and were superimposed by iron implants. A polyenergetic X-ray spectrum was generated by SpekCal software [54] for a tube voltage of 140 kVp, 2.5 mm aluminum filtration, 30° anode angle and a tube output of $\sim 200\ (\mu Gy)/(mAs)$ at 1 m. As shown in Fig. 5, the spectrum was uniformly sampled for 51 monoenergitic X-ray beams with an intensity and average energy calculated over each energy interval. For each beam, the energy-dependent linear attenuation coefficients of the classes were derived from the NIST XCOM photon cross section library [55]. The attenuation maps were forward projected and then the Poisson noise realization of the resulting sinograms were summed up to get a sinogram acquired under the polychromatic propagation of X-ray beams. The resulting sinogram was log-processed and reconstructed by FBP algorithm.

As shown in Fig. 4, the reconstructed artificial CT images suffer from streaking artifacts. In this simulation, scatters and nonlinear partial volume effect was not modeled. Following the generation of an artificially degraded image, we treated it as a really degraded CT image, from which we obtained a prior image, metallic implants, missing projections in the sinograms resulting from the polychromatic propagation of X-ray beams. In addition, for each dataset a ground truth image was obtained using the above-mentioned procedure by considering the metallic implants as bony structures.

In the simulated datasets, we evaluated the performance of the proposed L_0-DRS algorithm in comparison to conventional linear interpolation and the NMAR algorithm proposed by Meyer *et al.* [25]. In the objective comparison of MAR algorithms, two regions of interest (ROIs) were drawn on uncorrected images and the normalized root mean square difference (NRMSD) and mean absolute deviation (MAD) between corrected images (x^{MAR}) and their ground truth (x^{True}) were calculated for each ROI as follows:

$$\mathrm{NRMSD}(\%) = 100 \times \sqrt{\frac{\sum_{i\in \mathrm{ROI}} \left(x_i^{\mathrm{MAR}} - x_i^{\mathrm{True}}\right)^2}{\sum_{i\in \mathrm{ROI}} \left(x_i^{\mathrm{True}}\right)^2}}, \tag{17}$$

$$\mathrm{MAD}(\mathrm{HU}) = \frac{1}{N} \sum_{i\in \mathrm{ROI}} \left|x_i^{\mathrm{MAR}} - x_i^{\mathrm{True}}\right|. \tag{18}$$

For the clinical evaluation of the MAR algorithm, the CT datasets of eight patients were used. The data were acquired in helical mode on the Biograph 64 True Point PET/CT and Sensation 16 CT scanners (Siemens Healthcare, Erlangen, Germany), which have been respectively equipped with 40- and 24-row detectors. The datasets include: uni- and bi-lateral hip prostheses (two patients), dental fillings (three patients), spine fixation (one patient), and EEG electrodes (two patients). Table I summarizes the scanning parameters of the datasets. For quantitative evaluation of the MAR algorithms in these datasets, we calculated the

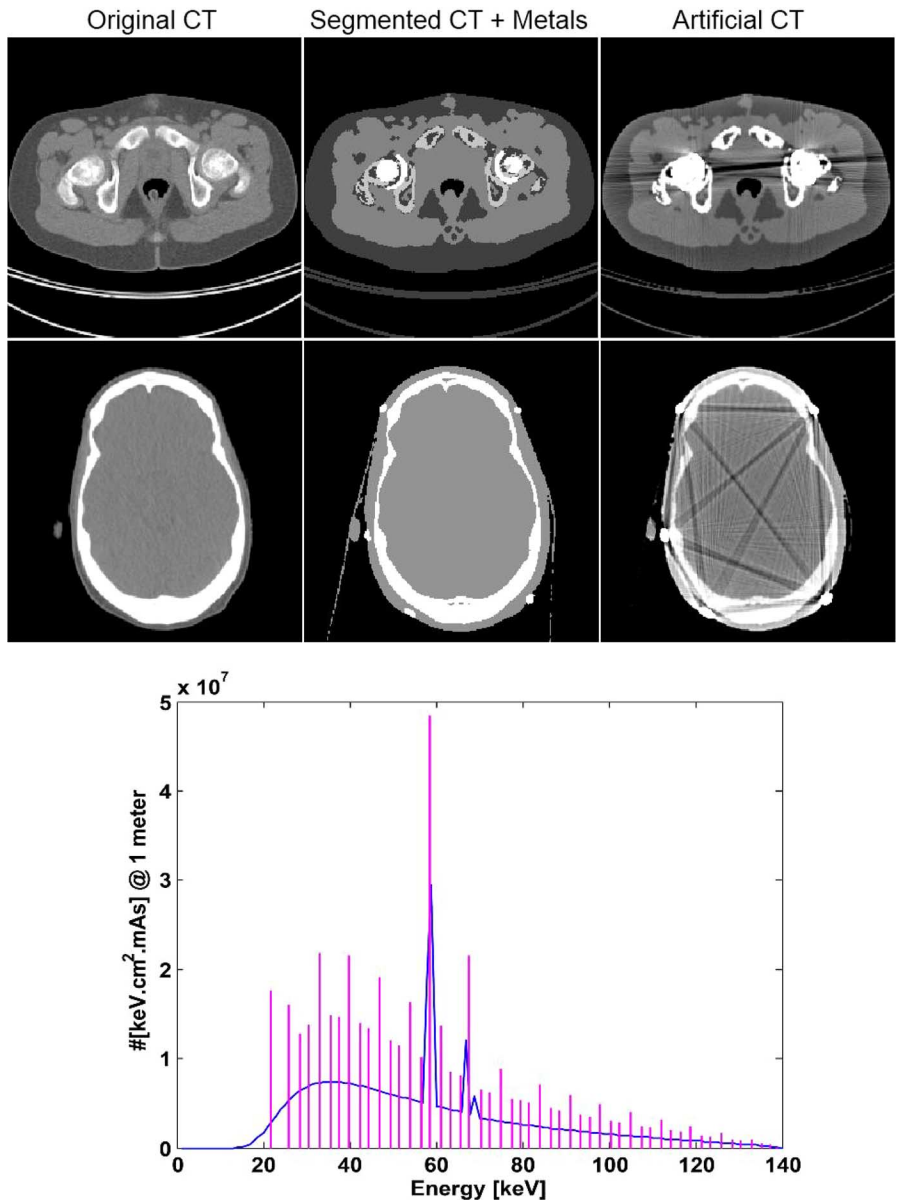

Fig. 4. Simulation of metal artifacts based on the polychromatic propagation of X-ray beams. Original CT images are segmented into different tissue classes and superimposed by metallic implants. The X-ray spectrum is sampled for a finite number of energies. The attenuation coefficients of each class is then calculated for each energy and the Poisson noise realization of their sinograms are then summed up and log-processed. The resulting sinograms are then reconstructed by FBP algorithm, which results in the artificial CT images with streaking artifacts. (Display window/level in first and second rows: 700/90 and 800/50 HU, respectively).

absolute mean deviation (AMD) between the mean CT numbers of two ROIs defined on uncorrected and corrected CT images over streaking artifacts. Owing to the absence of a ground truth in clinical datasets, we defined a same-size ROI on uncorrected images far from streaking artifacts and used it as a reference ROI.

III. Results

A. Simulation Studies

Fig. 5 shows the results of metal artifact reduction of the simulated bilateral hip and EEG head datasets using the studied MAR algorithms. In both datasets, the algorithms have noticeably reduced streaking artifacts. However, linear interpolation cannot effectively reduce the artifacts, since new artifacts have been introduced in the corrected images. The NMAR and proposed algorithms have noticeably reduced the artifacts, thereby improving the quality of the corrected images. In the hip dataset, the two algorithms depict nearly the same level of artifact reduction; however, as can be seen, the proposed algorithm tends also to restore the regions of metallic implants. In the head dataset, the proposed algorithm shows less residual artifacts in comparison with NMAR. Moreover, in this simulated dataset and also clinical datasets with EEG electrodes, we noticed that the NMAR algorithm introduces wide and severe bright streaking artifacts at the borders near the electrodes (see Fig. 5), which are due to the normalization of projection bins by small values at these regions. To practically reduce this effect in clinical datasets, we expanded the soft tissue region of prior images for this algorithm. Furthermore, to avoid division

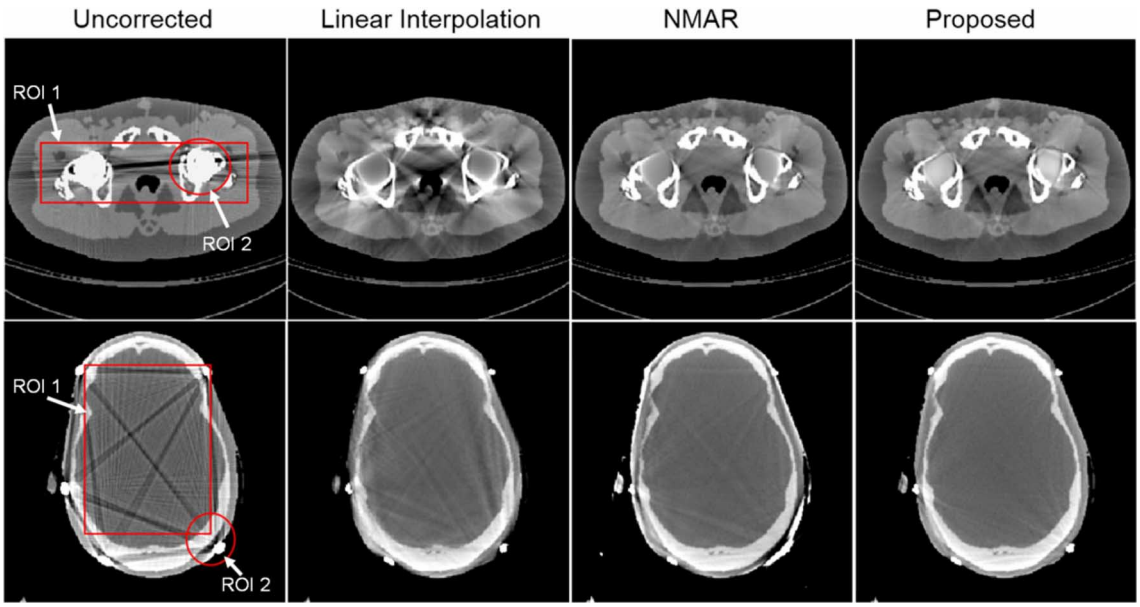

Fig. 5. Illustration of metal artifact reduction of simulated hip prostheses (top) and head EEG CT studies (bottom) (WW/WL $=500/50$ HU).

TABLE I
SUMMARY OF CT SCANNING PARAMETERS USED IN THE CLINICAL STUDIES

	Siemens Biograph 64 TP PET/CT			Siemens Sensation 16 CT	
	Hip prostheses	Dental fillings	Spine fixation	ECG electrodes	Dental fillings
Tube voltage (kVp)	100/120	120	120	140/120	120
Tube current (mA)	40/32	116/91	95	179/175	166
Exposure time (ms)	500	500	500/500	1500/1000	750
Slice thickness (mm)	2-2	5	5	3	5

TABLE II
ROI-BASED QUANTITATIVE EVALUATION OF THE STUDIED MAR ALGORITHMS USING SIMULATED HIP AND EEG CT STUDIES IN TERMS OF NRMSD AND MAD

Phantom	ROI	Uncorrected		Linear interpolation		NMAR		L_0-DRS	
		NRMSE (%)	MAD (HU)	NRMSE (%)	MAD (HU)	NRMSE (%)	MAD (HU)	NRMSE (%)	MAD (HU)
Hip prosthesis	1	56.96	197.29	13.43	109.12	7.53	54.78	7.27	55.50
	2	86.89	367.26	17.05	145.57	12.52	97.17	11.51	95.67
EEG electrodes	1	11.92	20.02	1.27	7.58	0.87	5.46	0.73	4.65
	2	73.03	145.73	8.83	43.49	31.07	151.94	3.58	19.79

by zero during normalization, we thresholded zero bins in the sinogram of the prior image at a threshold value $t = 1$. Small values of t have been suggested by Meyer *et al.* [25]; however, these values can result in highly inaccurate values in the normalized sinograms and hence can contribute to the appearance of severe bright streaking artifacts in the EEG datasets.

For quantitative comparison of the algorithms with respect to the ground truth image, two ROIs were defined on the degraded CT images (see Fig. 5, first column): one large rectangular ROI, namely ROI 1, to cover the most part of affected areas, and one circular ROI, namely ROI 2, for local evaluations near the implants. Table II summarizes the NRMSD and MAD results for the two datasets. In the ROI-based evaluations, the regions of metallic implants were excluded from the ROIs of (un-)corrected and ground truth images, since the implant are finally added back to the corrected images. The results of both datasets show that the proposed algorithm outperforms both linear interpolation and NMAR algorithms globally (in ROI 1) and locally (in ROI 2) through achieving lower NRMSD and MAD values. To further evaluate the algorithms, Fig. 6(a)–(c) shows three projection profiles on the sinograms of the hip dataset completed by the studied MAR algorithms along the dash lines shown in Fig. 6(d). As can be seen, the proposed MAR algorithm has more accurately estimated the missing projections toward the true projections.

For both simulated datasets, the relaxation parameter μ in Algorithm 1 was set to 0.8. To obtain this heuristically optimal value and also to evaluate the impact of μ on MAR performance and convergence rate of the proposed algorithm, we performed a set of experiments with different values of μ and monitored the variations of NRMSD in the defined ROIs. Fig. 7(a) and (b) shows NRMSD versus different values of μ in the range 0.65–0.95 with the increment value of 0.05 for ROIs 1 and 2, respectively. The results show that an optimal value of μ for these datasets is in the range 0.75–0.85. Thereby, we chose a mid value of 0.8 as an optimal value. The visual

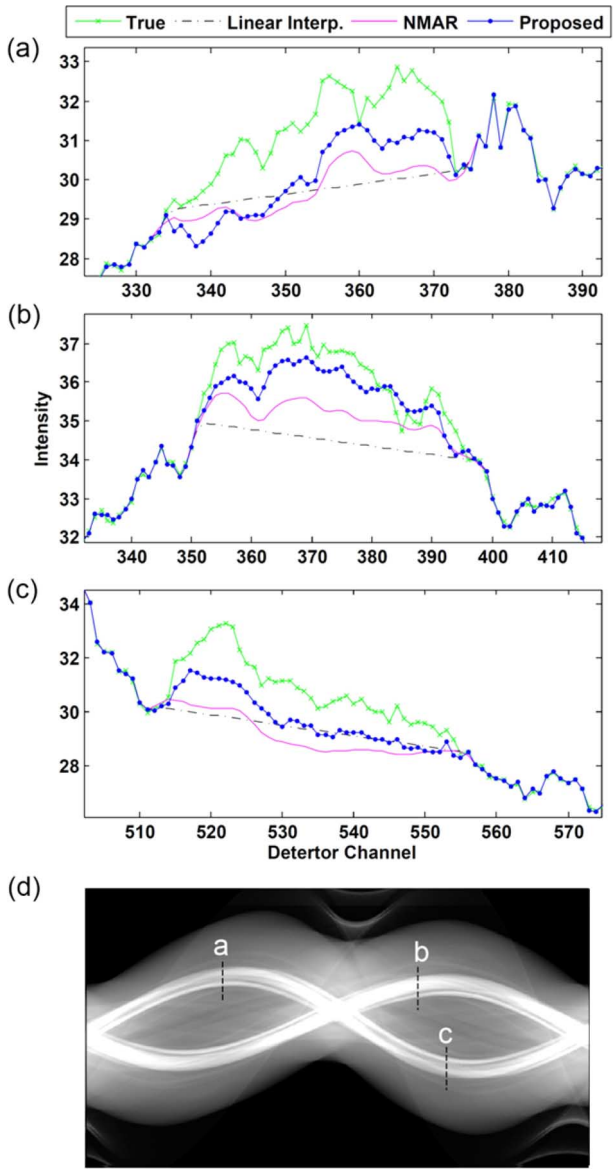

Fig. 6. Comparison of the projection profiles completed by the evaluated MAR algorithms with the true profiles of the hip prosthesis data along the dash lines shown in (d).

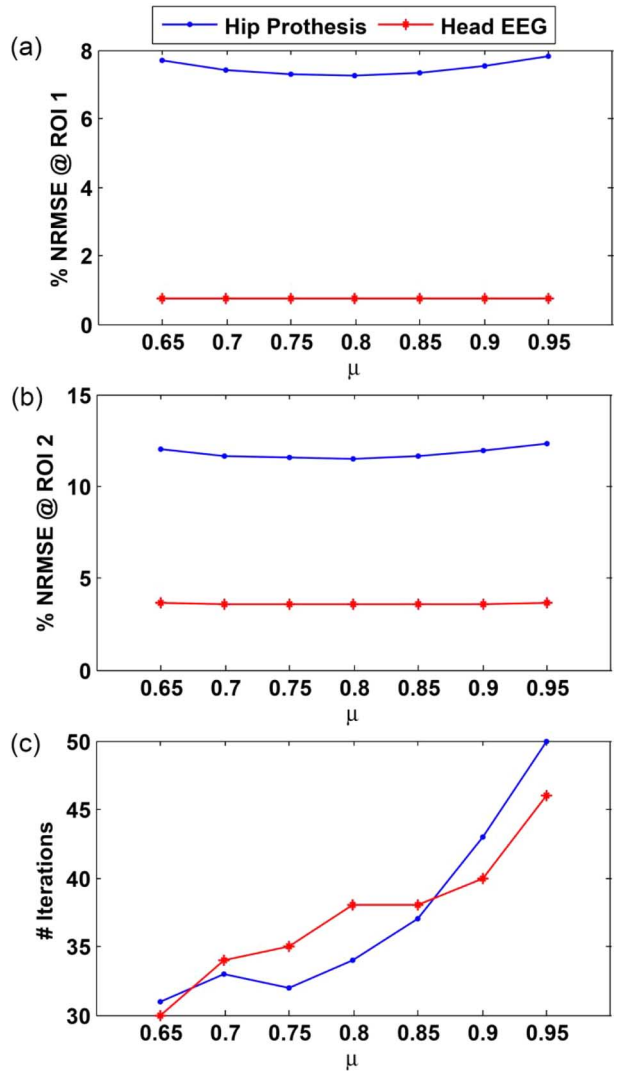

Fig. 7. Objective performance of the proposed L_0-DRS MAR algorithm for different relaxation parameters μ using the simulated hip and head CT data in terms of (a) and (b) NRMSD in ROIs 1 and 2, and (c) the number of required iterations to reach convergence.

comparison of the corrected images with different μ values did not reveal a significant difference.

The small variations of NRMSD of ROIs in both datasets, whose standard deviations are 0.01–0.2 in ROI 1 and 0.04–0.3 in ROI 2, reflect this observation. Fig. 7(c) shows the number of elapsed iterations for different values of the relaxation parameter. It turns out as μ increases the number of iterations also increases. In fact, for lower values of μ, the homotopic parameter ρ in (6) decays faster to zero, thereby the pseudo L_0 norm approaches an L_0 norm after fewer number of iterations. It should be emphasized that these results were obtained for a tolerance $\eta = 1 \times 10^{-3}$ in Algorithm 1. Therefore the algorithm was stopped when the relative difference between two successive wavelet coefficients is less than 1%. It was found that smaller tolerance values have no a significant effect on the quality of corrected images but can potentially increase the number of iterations and computation time. The average computational time of our MATLAB-based implementation of the proposed L_0-DRS algorithm was found to be around 5.1 seconds per iteration. Therefore, our simulation results show that higher values of μ and η might not be prudent in terms of image quality and computational time.

B. Clinical Studies

The simulated hip and EEG studies, which had different numbers and sizes of metallic implants, showed that the proposed algorithm achieves its best performance in terms of improvement of image quality and the required number of iterations when using $\mu = 0.8$ and $\eta = 1 \times 10^{-3}$. In our clinical studies, we initialized the proposed L_0-DRS algorithm using the above values and, similar to simulation studies, compared its performance against linear interpolation and NMAR algorithms. As mentioned earlier, four different categories of metallic implants, including hip prostheses, dental fillings, spine pedicle screw fixation and EEG electrodes were considered in this work. In each category, we selected three CT slices for qualitative evaluations.

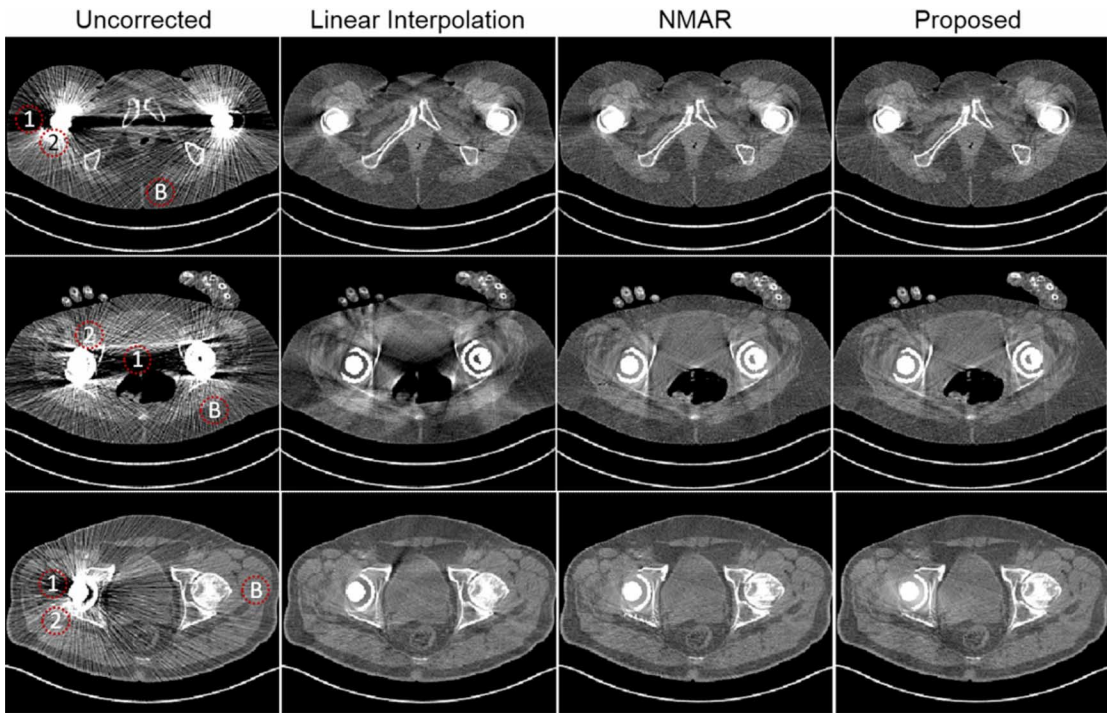

Fig. 8. Illustration of metal artifact reduction of the clinical hip prosthesis datasets (W W/WL $=700/40$ HU).

For each slice, three ROIs were defined on artifact degraded regions near metallic implants, namely ROIs 1 and 2, and on a background region far away from artifacts, namely ROI B and the absolute deviation between the mean CT number of ROIs 1 and 2 and that of ROI B was calculated.

1) Hip Prostheses: Fig. 8 shows the results of metal artifact reduction in CT slices of two patients with uni- and bi-lateral hip prostheses. As summarized in Table I, these patients have undergone a low-dose CT scan for attenuation correction as part of clinical PET/CT examinations. As can be seen, the metallic implants resulted in severe bright and streaking artifacts mostly due to beam hardening and photon starvation. The MAR algorithms have substantially reduced streaking artifacts. However, linear interpolation has introduced new artifacts, especially in the second-row dataset in which there are two large hip prostheses that corrupt a large number of projections, which makes pure interpolation inefficient. The NMAR algorithm improves the performance of linear interpolation by normalization with a prior sinogram. In comparison, it has remarkably improved image quality; however, there are still residual dark and new bright artifacts in the first- and second-row images. The proposed wavelet-based MAR algorithm, which incorporates the same prior sinogram as in NMAR, has also improved image quality and visually achieved the same level of artifact reduction as NMAR. However, a close inspection revealed that the proposed algorithm has reduced more effectively the residual dark streaking artifacts in the first-row image and has introduced less bright artifacts in the second-row image around the implants. For the quantitative evaluation of the algorithms, we delineated ROIs 1, 2, and B on the uncorrected image, as shown in Fig. 8, first column. The ROIs are of the same size, 30 mm in diameter. Since in this case, ROI B contains streaking artifacts, we used the NMAR image as a reference for this background ROI. The quantitative results are presented in Table III. Note in this table the cases 1–3 correspond to the images shown in first to third rows. The results show the proposed algorithm generally achieves lower AMD values compared to NMAR algorithm in both ROIs that were defined in regions impaired with dark streaking artifacts. It should be noted that in the third case, linear interpolation outperforms the other algorithms algorithm; however, in terms of overall image quality, the proposed and NMAR have a better performance.

2) Dental Fillings: The reduction of artifacts arising from dental fillings is a challenging task because there are often multiple high-density implants that severely corrupt projection data and thereby the resulting streaking artifacts obscure diagnostically important information in the dental arch area. Fig. 9 shows the results of artifact reduction in CT data of three patients presenting with dental fillings. As can be seen, linear interpolation introduced new streaking artifacts in all three cases. Because, as mentioned above, in such cases there are multiple closely-seated dental fillings which make pure interpolation of corrupted projections from neighboring projections inefficient and even inaccurate. The images corrected by NMAR and the proposed algorithm show a substantial improvement in artifacts reduction without introducing new severe ones. Note that in the case of the first and second row datasets, we applied a dilation morphological filtering (with disk-shaped structuring element of 1.94 mm radius) to the segmented metallic implants in order to completely remove residual artifacts in the images corrected by NMAR and proposed MAR algorithms. Afterwards, the original segmented metals were added back to the images. The comparison of results in the first-row dataset, which has been acquired with arms up, shows that the proposed algorithm

TABLE III
ROI-BASED QUANTITATIVE EVALUATION OF THE STUDIED MAR ALGORITHMS IN THE CLINICAL CASES, SHOWN IN FIGS. 9–11, IN TERMS OF AMD BETWEEN THE MEAN CT NUMBER OF TWO ROIS, DRAWN ON ARTIFACT REGIONS (NAMELY, ROI 1 AND 2), AND THAT OF A REFERENCE ROI, DRAWN ON A BACKGROUND REGION FAR FROM ARTIFACTS (NAMELY ROI B). FOR EACH DATASET, THE CT IMAGES OF CASES 1–3 HAVE, RESPECTIVELY, BEEN SHOWN IN THE FIRST TO THIRD ROWS OF THE FIGURES

Dataset	Case #	ROI #	Uncorrected	Linear interpolation	NMAR	L_0-DRS
Hip prosthesis	1	1	347.41	87.62	73.57	52.18
		2	576.97	178.94	181.00	173.41
	2	1	153.08	104.53	145.78	124.44
		2	303.30	247.32	113.45	108.81
	3	1	146.73	14.73	26.11	53.14
		2	145.59	5.95	22.33	7.55
Dental fillings	1	1	89.60	99.17	155.86	46.91
		2	73.51	6.65	12.23	0.00
	2	1	54.53	52.48	56.55	36.64
		2	187.25	81.55	73.93	66.11
	3	1	76.54	78.54	22.58	60.65
		2	59.94	54.56	15.92	1.01
Spine fixation	1	1	92.39	98.75	4.22	4.90
		2	43.68	15.03	42.60	6.04
	2	1	200.96	67.98	21.13	19.88
		2	4.05	82.41	76.78	56.96
	3	1	113.42	92.40	59.41	52.01
		2	134.91	64.89	25.42	20.59
EEG electrodes	1	1	0.16	3.69	11.45	8.90
		2	2.29	13.16	10.32	0.49
	2	1	54.02	19.34	23.54	20.51
		2	27.13	74.45	38.05	3.14
	3	1	54.38	121.40	88.09	62.94
		2	12.95	40.10	24.09	18.83

outperforms its NMAR counterpart by the reduction of artifacts without introducing new blurring-like artifacts in the palatine area. In the second-row dataset, the same trend is also observed, although the performance of the algorithms is more comparable. In the third-row dataset, the proposed algorithm has, however, slightly introduced new bright streaking artifacts in the area between the implants. For quantitative comparison of the algorithms, three ROIs (20 mm in diameter) were defined on the uncorrected images, as shown in Fig. 9. The results of ROI analysis show that the L_0-DRS algorithm outperforms the NMAR algorithm by achieving lower values of absolute mean deviation with respect to the background ROI B.

3) Spine Fixation: Fig. 10 shows the results of metal artifact reduction in three CT slices of a patient with spine fixation undergoing low-dose CT imaging in the context of a PET/CT examination. The results show that the reduction of artifacts in this localization is somehow challenging, since the implants are seated close together and several bony structures surround the implants. In all three cases, linear interpolation is not efficient and introduces new streaking artifacts. In the first-row dataset, the NMAR and proposed algorithms substantially suppress dark streaking artifacts; however, both of them have introduced blurring and new artifacts around and beneath the implants. In the second- and third-row datasets, both algorithms have noticeably reduced the artifacts in comparison with linear interpolation, particularly in the last one, where both algorithms have almost eradicated the artifacts. The quantitative evaluation of the algorithms was performed using the same-size (20 mm in diameter) ROIs. The results have been summarized in Table III. It turns out that the proposed algorithm can generally outperform NMAR, which can be verified by visual interpretation of the corrected images in for example ROI 2 of first-row dataset. As can be seen, the proposed algorithm has comparably introduced less dark artifacts in that region.

4) EEG Electrodes: Fig. 11 shows the results of metal artifact reduction of the CT data presenting with EEG electrodes. As expected, linear interpolation lags behind NMAR and the proposed algorithm since they make use of some prior information during projection completion. In the first- and second-row datasets, a morphological dilation filtering (with a disk element of radius 1.94 mm) was applied on the segmented metallic implants, because our preliminary results showed that simple thresholding cannot guarantee the identification of all corrupted projections and thereby dark streaking artifacts reappear in the reconstructed images. As mentioned earlier, in the case of NMAR algorithm, the soft tissue portion of the prior images of the datasets was expanded by a dilation filtering, as this algorithm results in extremely severe bright artifacts at the borders. The results show that in all three datasets, the proposed algorithm outperforms its counterparts. The outperformance of this algorithm is more noticeable in the amount of residual artifacts in the cranium area. More accurate artifact reduction in regions close to electrodes is achieved by the proposed algorithm.

As can be seen, linear interpolation and NMAR algorithms have respectively distorted and underestimated soft tissues around the electrodes. The quantitative analysis was performed

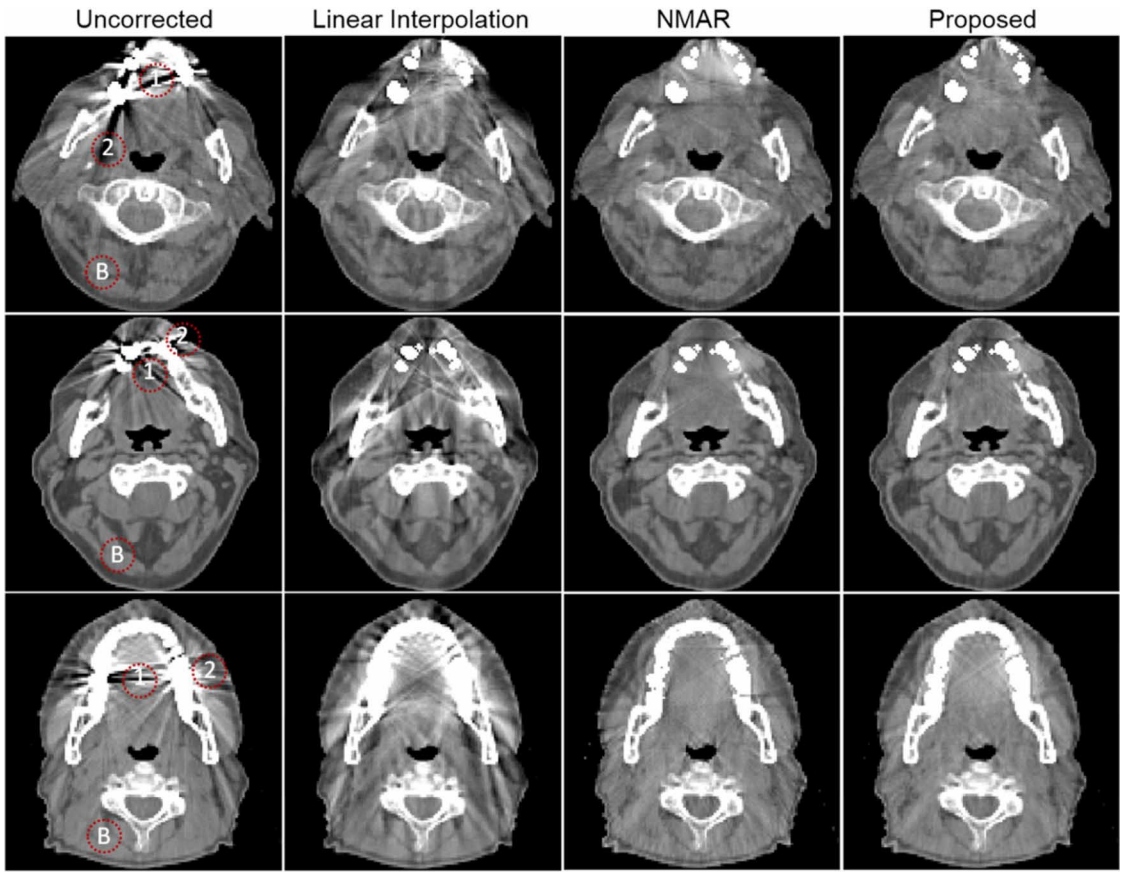

Fig. 9. Illustration of metal artifact reduction of clinical dental filling CT data (WW/WL $=600/40$ HU).

for same-size ROIs (30 mm in diameter) shown in Fig. 11, first column. The results presented in Table III show that the proposed algorithm achieves lower metric values, resulting from the introduction of less artifacts in this region.

To further assess the performance of the studied algorithms in the sinogram domain, Fig. 12 compares the sinograms of uncorrected and corrected images of two datasets. The first row shows the sinograms of the bilateral hip dataset shown in Fig. 8 (middle row), while the second one shows those of the EEG electrode dataset shown in Fig. 11 (middle row). In both cases, the sinograms with missing projections (metal traces) have also been shown. As can be seen, linear interpolation simply bridges the missing area and results in discontinuities. This inaccurate projection completion also appears in the NMAR algorithm, especially in the second-row sinogram, where in some projection angles the missing projections are close to the border of the head. In both datasets, the proposed algorithm has more accurately and continuously estimated the missing projections.

IV. Discussion

The presence of permanent metallic implants in patients undergoing X-ray CT imaging can induce streaking metal artifacts that impair the diagnostic quality and clinical usefulness of CT images. In this work, we proposed a new projection completion based MAR algorithm by formulating the recovery of missing projections as a regularized inverse problem and employed a pseudo L_0 sparsity-promoting prior to impose the prior knowledge of the sparsity CT sinograms in a dictionary of translation invariant wavelets. Furthermore, we exploited the detail sub-bands of the wavelet coefficients of a prior sinogram to improve the efficiency of the proposed algorithm.

We compared the proposed algorithm with linear interpolation and Meyer's NMAR algorithms. The NMAR algorithm uses prior sinogram for normalizing and flattening the neighboring projections of missing regions, thus facilitating the interpolation task. In contrast, our proposed algorithm is based on solving an optimization problem in which the missing projections are iteratively estimated. In this algorithm, the prior sinograms are exploited in a very different approach. The detail wavelet coefficients of a prior sinogram are iteratively introduced into this algorithm during the pseudo L_0-based thresholding of intermediate wavelet coefficients (see Algorithm 1). Following the convergence of the algorithm, declared by a stopping criterion, an inverse wavelet transform is applied on the estimated coefficients and the completed sinogram is obtained. Zhao *et al.* [11] proposed a related projection completion MAR algorithm in the wavelet domain. In this algorithm, the missing projections are one-dimensionally interpolated by a weighted sum of the wavelet coefficients of the corrupted projections and the wavelet coefficients of linearly interpolated projections. Although theoretically well-founded, this algorithm did not significantly reduce metal artifacts compared to standard linear interpolation. In contrast, the proposed algorithm is an iterative wavelet-based algorithm in which missing projections are two-

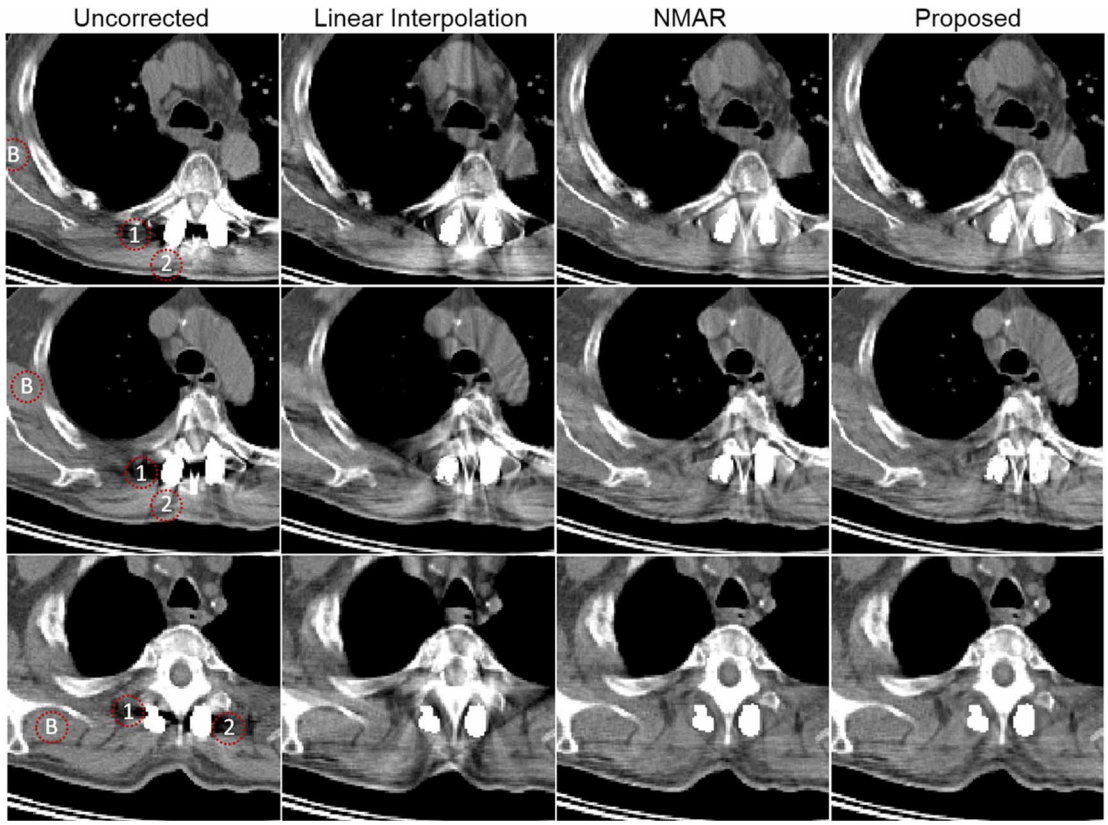

Fig. 10. Illustration of metal artifact reduction of clinical spine fixation CT data (WW/WL $=500/40$ HU).

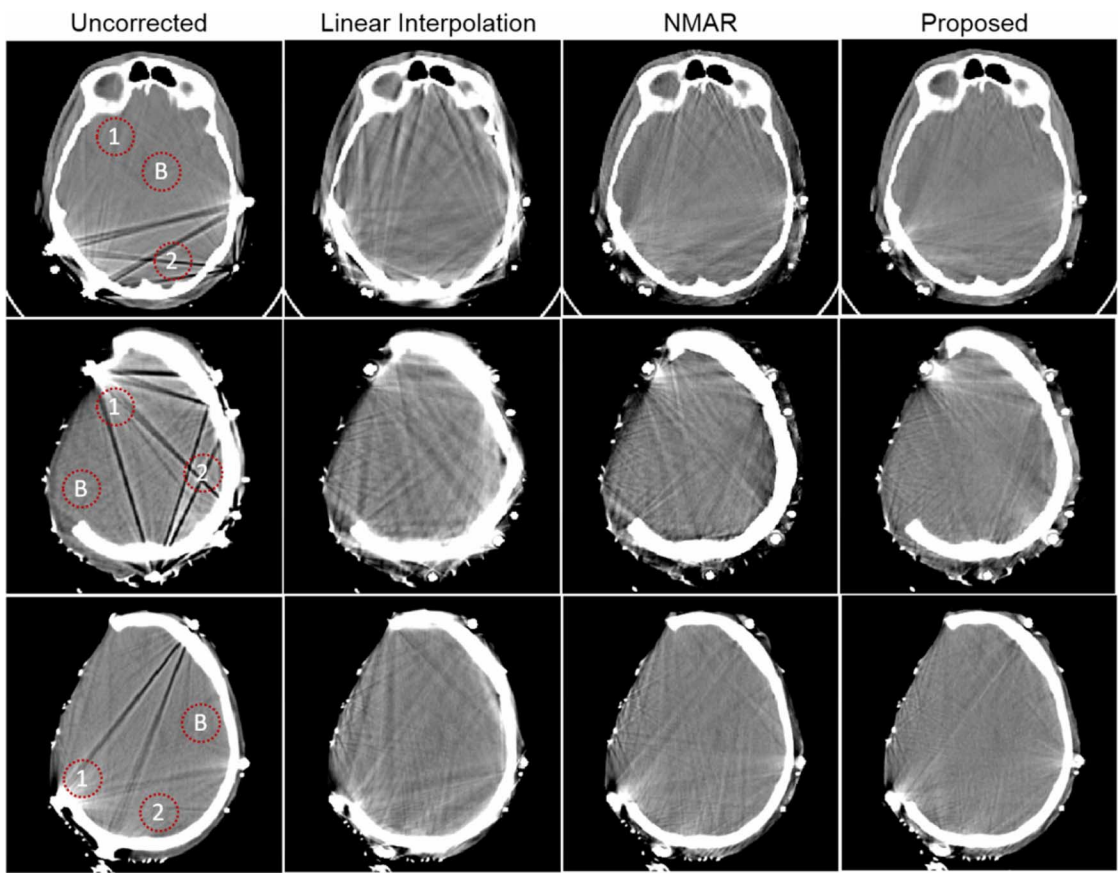

Fig. 11. Illustration of metal artifact reduction of clinical head EEG studies (WW/WL $=500/40$ HU). The results show that the proposed algorithm results in the lowest residual artifacts, especially at the borders near to the electrodes.

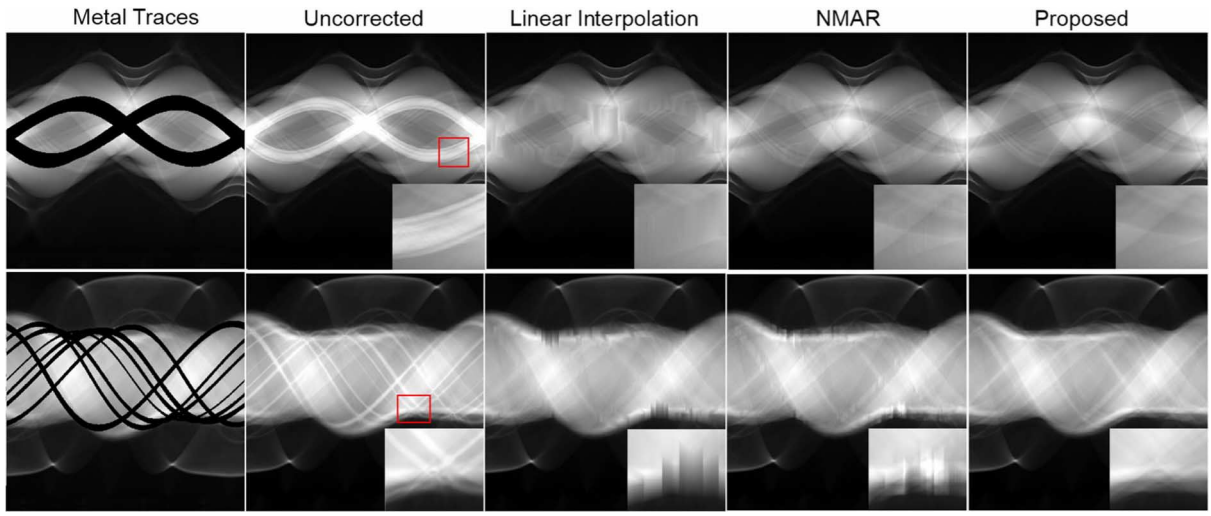

Fig. 12. Comparison of the sinograms completed by the studied MAR algorithms. Top to bottom: the sinograms of the images shown in the middle row of Figs. 8 and 11, respectively. In first column, the missing projections (metal traces) have been shown with zero-intensity.

dimensionally optimally estimated by thresholding and proximal mapping schemes.

To objectively assess the efficacy of the proposed algorithm with respect to a ground truth, we simulated metal artifacts in tissue-segmented CT datasets by considering the polychromatic propagation of X-ray beams. As can be seen in Fig. 4, the resulting streaking artifacts impair the tissues in the same way as a real CT acquisition. Although in this simulation the generation of streaking artifacts due to scatters and nonlinear partial effect was not modeled, it provided us with a ground truth and an artificially degraded image. Thereby, the performance of the algorithms was evaluated for a data recovery problem in which the amount of missing data and the source of available data are the same. Moreover, as the simulations were performed on phantoms derived from clinical cases, the impact of the relaxation parameter μ on the performance of the proposed algorithm could be objectively optimized and used in our clinical studies. Despite the absence of ground truth for patients with metallic implants, we also followed an ROI-based quantitative evaluation approach for the evaluation of MAR algorithms using clinical datasets and reference ROIs defined on uncorrected images. It is worth nothing that there are few reference-free criteria such as band-pass filtered gradient (BPG) [56] and regression without truth (RWT) [57], which can be respectively used to evaluate the performance of MAR algorithms in the sinogram domain and on images of a population of patients [58]. However, these methods need for optimization tasks and parameter selections, which complicate the evaluation procedure.

In both simulated and clinical studies, the segmentation of uncorrected images to produce metallic implants and prior images were performed by simply thresholding. The dark and bright artifacts falsely segmented as air and bone regions were eliminated by close and open morphological filtering. The accuracy of the prior image is of great importance for the performance of both NMAR and the proposed algorithm, since segmentation errors in prior image can reappear in final reconstructions. For accurate segmentation of artifacts from anatomy in a prior image, automatic procedures through adaptive and knowledge-based thresholding have been described in [59] and [60], respectively.

The evaluation of the proposed L_0-DRS algorithm against linear interpolation and NMAR algorithms using various simulated and clinical datasets showed that our algorithm can outperform its counterparts objectively and subjectively and therefore reduce metal artifacts in a more efficient way. Its improved performance should be ascribed to the facts that this wavelet-based MAR algorithm decomposes a sinogram into several resolution levels and estimate the missing projections in approximate and detail sub-bands through a thresholding scheme guided by prior wavelet coefficients. One of the current limitations of the proposed algorithm in comparison with NMAR is computational time. In this study, we exploited translation invariant wavelets implemented by undecimated discrete wavelet transform (UDWT). In this implementation, the decimation (down sampling) is eliminated in favor of invariance to the shifts of an input image, thus avoiding the star-like artifacts usually induced by the standard decimated wavelet transform. However, due to its redundancy, the UDWT is of higher computational complexity and renders the computational cost of our iterative MAR algorithm relatively expensive. The average computation time of the algorithm in the clinical datasets was found to be about 5 min. In this work, the performance of the proposed algorithm was evaluated for four resolution levels yielding a redundancy factor of 1:13, since there are three detail sub-bands for each resolution level (in horizontal, vertical and diagonal directions) and one approximation sub-band for all levels. In addition, we followed a block-wise recovery of missing projections in the wavelet domain. For each sinogram, two overlapping 512×512 blocks were considered, therefore the matrix size of UDWTs became $512 \times 512 \times 13 \times 2$, which obviously calls for an increased number of arithmetic operations. Future work will focus on decreasing the computational burden of the algorithm by: 1) performance and trade-off assessment of the algorithm for lower resolutions and use of other wavelets such as Daubechies wavelets with a vanishing moment of 4, 2) employing smaller

block sizes, and 3) implementation of UDWT in MATLAB MEX file or C/C++. In addition, future work will concentrate on improving the performance of the proposed algorithm by utilizing modified sub-bands of the corrupted sinograms to better preserve the edge information around metallic implants.

V. Conclusion

In this study, an L_0 wavelet-based projection completion algorithm was proposed for metal artifact reduction in X-ray CT imaging. In this algorithm, the completion of missing projections was formulated as regularized inverse problem which was solved using the Douglas–Rachford splitting algorithm. The sparsity of the wavelet coefficients of CT sinograms as well as the detail wavelet coefficients obtained from the segmentation of the uncorrected images were exploited in the algorithm as prior information. The performance of the proposed L_0-DRS MAR algorithm was compared with conventional linear interpolation and the normalized MAR algorithm proposed by Meyer *et al.* [25]. It was demonstrated that in simulation and clinical studies the proposed algorithm can outperform it counterparts based on objective and subjective metrics. In conclusion, the proposed MAR algorithm proved to be promising in reducing metal artifacts in X-ray CT imaging.

Appendix A

To solve the problem in (13) for the quasi-convex log function, we follow the proof of proposition 1 in [61]. When $z_i = 0$, it is clear that the unique minimizer is $\hat{z}_i \triangleq \text{prox}_{\lambda\psi}(\theta_i)$ is zero. Moreover, as the log potential function

$$\psi(z_i) = \nu \ln\left(1 + \frac{|z_i|}{\rho}\right), \quad \nu = \ln\left(1 + \frac{1}{\rho}\right)^{-1}$$

is even-symmetric, therefore the minimizer of this problem is odd, i.e., $\text{prox}_{\lambda\psi}(-\theta_i) = -\text{prox}_{\lambda\psi}(\theta_i)$, and one can only consider $z_i > 0$. By equating the derivative of the objective of the problem to zero, i.e.,

$$z_i - \theta_i + \lambda\nu(z_i + \rho)^{-1} = 0$$

a quadratic equation is obtained, whose real positive root is given by

$$\text{prox}_{\lambda\psi}(\theta_i) = \frac{1}{2}(\theta_i - \rho + \sqrt{(\theta_i + \rho)^2 - 4\lambda\nu}) \qquad \text{(A1)}$$

if $\theta_i > (2\sqrt{\lambda\nu} - \rho)$. For $z_i < 0$, one can exploit the oddness property of this solution, thereby the minimizer of the problem reads: $-\text{prox}_{\lambda\psi}(-\theta_i)$ if $\theta_i < -(2\sqrt{\lambda\nu} - \rho)$. From above, it is deduced that in the interval $|\theta_i| < (2\sqrt{\lambda\nu} - \rho)$, z_i and thus $\text{prox}_{\lambda\psi}(\theta_i)$ are zero. Hence, the solution is obtained as in (14). When $\rho \to \infty$, the equation in (A1) asymptotically approaches $\text{prox}_{\lambda\psi}(\theta_i) = \theta_i - \lambda$ with real positive values for $\theta_i > \lambda$, which gives rise to a *soft* thresholding rule as follows:

$$\text{prox}_{\lambda\psi}(\theta_i) = \begin{cases} \theta_i - \lambda, & \theta_i > \lambda \\ 0, & |\theta_i| \le \lambda \\ \theta_i + \lambda, & \theta_i < -\lambda \end{cases}. \qquad \text{(A2)}$$

References

[1] W. R. Hendee and E. R. Ritenour, *Medical Imaging Physics*, 4th ed. New York: Wiley-Liss, 2002.

[2] J. Hsieh, *Computed Tomography: Principles, Design, Artifacts, and Recent Advances*, 2nd ed. Bellingham, WA: SPIE, 2009.

[3] M. Abdoli, R. A. J. O. Dierckx, and H. Zaidi, "Metal artifact reduction strategies for improved attenuation correction in hybrid PET/CT imaging," *Med. Phys.*, vol. 39, no. 6, pp. 3343–3360, 2012.

[4] W. A. Kalender, R. Hebel, and J. Ebersberger, "Reduction of CT artifacts caused by metallic implants," *Radiology*, vol. 164, no. 2, pp. 576–577, 1987.

[5] J. Wei, G. A. Sandison, W.-C. Hsi, M. Ringor, and X. Lu, "Dosimetric impact of a CT metal artefact suppression algorithm for proton, electron and photon therapies," *Phys. Med. Biol.*, vol. 51, no. 20, pp. 5183–5197, 2006.

[6] M. R. Ay, A. Mehranian, M. Abdoli, P. Ghafarian, and H. Zaidi, "Qualitative and quantitative assessment of metal artifacts arising from implantable cardiac pacing devices in oncological PET/CT studies: A phantom study," *Mol. Imag. Biol.*, vol. 13, no. 6, pp. 1077–1087, 2011.

[7] B. De Man, J. Nuyts, P. Dupont, G. Marchal, and P. Suetens, "Metal streak artifacts in X-ray computed tomography: A simulation study," in *Proc. IEEE Nucl. Sci. Symp. Conf. Rec.*, 1998, pp. 1860–1865.

[8] J. Wei, L. Chen, G. A. Sandison, Y. Liang, and L. X. Xu, "X-ray CT high-density artefact suppression in the presence of bones.," *Phys. Med. Biol.*, vol. 49, no. 24, pp. 5407–5418, 2004.

[9] M. Abdoli, M. R. Ay, A. Ahmadian, and H. Zaidi, "A virtual sinogram method to reduce dental metallic implant artefacts in computed tomography-based attenuation correction for PET.," *Nucl. Med. Commun.*, vol. 31, no. 1, pp. 22–31, 2010.

[10] C. Xu, F. Verhaegen, D. Laurendeau, S. A. Enger, and L. Beaulieu, "An algorithm for efficient metal artifact reductions in permanent seed," *Med. Phys.*, vol. 38, no. 1, pp. 47–56, 2011.

[11] S. Zhao, D. D. Robertson, G. Wang, B. Whiting, and K. T. Bae, "X-ray CT metal artifact reduction using wavelets: An application for imaging total hip prostheses," *IEEE Trans. Med. Imag.*, vol. 19, no. 12, pp. 1238–1247, Dec. 2000.

[12] E. M. Abu Anas, S. Y. Lee, and M. K. Hasan, "Removal of ring artifacts in CT imaging through detection and correction of stripes in the sinogram.," *Phys. Med. Biol.*, vol. 55, no. 22, pp. 6911–6930, 2010.

[13] W. J. H. Veldkamp, R. M. S. Joemai, A. J. van der Molen, and J. Geleijns, "Development and validation of segmentation and interpolation techniques in sinograms for metal artifact suppression in CT," *Med. Phys.*, vol. 37, no. 2, pp. 620–628, 2010.

[14] J. Gu, L. Zhang, G. Yu, Y. Xing, and Z. Chen, "X-ray CT metal artifacts reduction through curvature based sinogram inpainting.," *J. X-ray Sci. Technol.*, vol. 14, pp. 73–82, 2006.

[15] X. Duan, L. Zhang, Y. Xiao, J. Cheng, Z. Chen, and Y. Xing, "Metal artifact reduction in CT images by sinogram TV inpainting," in *IEEE Nucl. Sci. Symp. Conf. Rec.*, 2008, pp. 4175–4177.

[16] H. Xue, L. Zhang, Y. Xiao, Z. Chen, and Y. Xing, "Metal artifact reduction in dual energy CT by sinogram segmentation based on active contour model and TV inpainting," in *IEEE Nucl. Sci. Symp. Conf. Rec.*, 2009, pp. 904–908.

[17] Y. Zhang, Y. F. Pu, J. R. Hu, Y. Liu, and J. L. Zhou, "A new CT metal artifacts reduction algorithm based on fractional-order sinogram inpainting," *J. X-ray Sci. Technol.*, vol. 19, no. 3, pp. 373–384, 2011.

[18] M. Yazdi, M. A. Lari, G. Bernier, and L. Beaulieu, "An opposite view data replacement approach for reducing artifacts due to metallic dental objects.," *Med. Phys.*, vol. 38, no. 4, pp. 2275–2281, 2011.

[19] S. Tohnak, A. J. H. Mehnert, M. Mahoney, and S. Crozier, "Dental CT metal artefact reduction based on sequential substitution.," *Dentomaxillofac Radiol.*, vol. 40, no. 3, pp. 184–190, 2011.

[20] B. Kratz, I. Weyers, and T. M. Buzug, "A fully 3D approach for metal artifact reduction in computed tomography," *Med. Phys.*, vol. 39, no. 11, pp. 7042–7054, 2012.

[21] M. Bal and L. Spies, "Metal artifact reduction in CT using tissue-class modeling and adaptive prefiltering.," *Med. Phys.*, vol. 33, no. 8, pp. 2852–2859, 2006.

[22] H. Yu, K. Zeng, D. K. Bharkhada, G. Wang, M. T. Madsen, O. Saba, B. Policeni, M. A. Howard, and W. R. Smoker, "A segmentation-based method for metal artifact reduction," *Acad. Radiol.*, vol. 14, no. 4, pp. 495–504, 2007.

[23] D. Prell, Y. Kyriakou, M. Beister, and W. A. Kalender, "A novel forward projection-based metal artifact reduction method for flat-detector computed tomography.," *Phys. Med. Biol.*, vol. 54, no. 21, pp. 6575–6591, 2009.

[24] M. Meilinger, C. Schmidgunst, O. Schutz, and E. W. Lang, "Metal artifact reduction in cone beam computed tomography using forward projected reconstruction information," *Z. Med. Phys.*, vol. 21, no. 3, pp. 174–182, 2011.

[25] E. Meyer, R. Raupach, M. Lell, B. Schmidt, and M. Kachelriess, "Normalized metal artifact reduction (NMAR) in computed tomography," *Med. Phys.*, vol. 37, no. 10, pp. 5482–5493, 2010.

[26] M. Abdoli, M. Ay, A. Ahmadian, R. Dierckx, and H. Zaidi, "Reduction of dental filling metallic artefacts in CT-based attenuation correction of PET data using weighted virtual sinograms optimized by a genetic algorithm," *Med. Phys.*, vol. 37, no. 12, pp. 6166–6177, 2010.

[27] X. Zhang, J. Wang, and L. Xing, "Metal artifact reduction in X-ray computed tomography (CT) by constrained optimization.," *Med. Phys.*, vol. 38, no. 2, pp. 701–711, 2011.

[28] A. P. Dempster, N. M. Laird, and D. B. Rubin, "Maximum likelihood from incomplete data via the EM algorithm.," *J. R. Stat. Soc. B*, vol. 38, pp. 1–38, 1977.

[29] B. De Man, "Iterative reconstruction for reduction of metal artifact in computed tomography," Ph.D. dissertation, Morfologie En Medsiche, Katholieke Universiteit Leuven, Leuven, Belgium, 2001.

[30] M. Oehler and T. M. Buzug, "Statistical image reconstruction for inconsistent CT projection data," *Methods Inf. Med.*, vol. 46, pp. 261–269, 2007.

[31] L. Ritschl, F. Bergner, C. Fleischmann, and M. Kachelrieß, "Improved total variation-based CT image reconstruction applied to clinical data.," *Phys. Med. Biol.*, vol. 56, pp. 1545–1561, 2011.

[32] H. Xue, L. Zhang, Y. Xing, and Z. Chen, "An iterative reconstruction technique for metal artifact reduction," in *Proc. 11th Fully Three-Dimensional Image Reconstruct. Radiol. Nucl. Med.*, Potsdam, Germany, 2011, pp. 199–202.

[33] B. Meng, J. Wang, and L. Xing, "Sinogram preprocessing and binary reconstruction for determination of the shape and location of metal objects in computed tomography (CT)," *Med. Phys.*, vol. 37, no. 11, pp. 5867–5875, 2010.

[34] J. Choi, K. S. Kim, M. W. Kim, W. Seong, and J. C. Ye, "Sparsity driven metal part reconstruction for artifact removal in dental CT.," *J. X-ray Sci. Tech.*, vol. 19, pp. 457–475, 2011.

[35] J. F. Williamson, B. R. Whiting, J. Benac, R. J. Murphy, G. J. Blaine, J. A. O'Sullivan, D. G. Politte, and D. L. Snyder, "Prospects for quantitative computed tomography imaging in the presence of foreign metal bodies using statistical image reconstruction," *Med. Phys.*, vol. 29, no. 10, pp. 2404–2418, 2002.

[36] C. Lemmens, D. Faul, and J. Nuyts, "Suppression of metal artifacts in CT using a reconstruction procedure that combines MAP and projection completion.," *IEEE Trans. Med. Imag.*, vol. 28, no. 2, pp. 250–260, Feb. 2009.

[37] K. Van Slambrouck and J. Nuyts, "Metal artifact reduction in computed tomography using local models in an image block-iterative scheme," *Med. Phys.*, vol. 39, no. 11, pp. 7080–7093, 2012.

[38] M. Elad*, Sparse and Redundant Representations, From Theory to Applications in Signal and Image Processing*. New York: Springer, 2010.

[39] I. Daubechies, B. Han, A. Ron, and Z. Shen, "Framelets: MRA-based constructions of wavelet frames," *Appl. Comput. Harmon. Anal.*, vol. 14, no. 1, pp. 1–46, 2003.

[40] H. Ji, Z. Shen, and Y. Xu, "Wavelet frame based image restoration with missing/damaged pixels," *East Asia J. Appl. Math.*, vol. 1, pp. 108–131, 2011.

[41] M. Elad, P. Milanfar, and R. Rubinstein, "Analysis versus synthesis in signal priors," *Inverse Problems*, vol. 23, no. 3, pp. 947–968, 2007.

[42] A. Skodras, C. Christopoulos, and T. Ebrahimi, "The JPEG 2000 still image compression standard," *IEEE Signal Process. Mag.*, vol. 18, no. 5, pp. 36–58, Sep. 2001.

[43] P. Moulin and J. Liu, "Analysis of multiresolution image denoising schemes using generalized-Gaussian and complexity priors," *IEEE Trans. Inf. Theory*, vol. 45, no. 3, pp. 909–919, Apr. 1999.

[44] S. S. Chen, D. Donoho, L. , M. Saunders, and A. , "Atomic decomposition by basis pursuit.," *SIAM J. Sci. Comput.*, vol. 20, no. 1, pp. 33–61, 1998.

[45] D. L. Donoho, "Compressed sensing," *IEEE Trans. Inf. Theory*, vol. 52, no. 4, pp. 1289–1306, 2006.

[46] E. Candes, M. Wakin, and S. Boyd, "Enhancing sparsity by reweighted l1 mm Minimization," *J. Fourier Anal. Appl.*, no. 14, pp. 877–905, 2007.

[47] J. Trzasko and A. Manduca, "Highly undersampled magnetic resonance image reconstruction via homotopic $\ell 0$-minimization," *IEEE Trans. Med. Imag.*, vol. 28, no. 1, pp. 106–121, Jan. 2009.

[48] P. L. Combettes and J. C. Pesquet, "A Douglas-Rachford splitting approach to nonsmooth convex variational signal recovery," *IEEE J. Sel. Topics Signal Process.*, vol. 1, no. 4, pp. 564–574, 2007.

[49] I. Ekeland and R. Temam*, Convex Analysis and Variational Problems*. Amsterdam, The Netherlands: North-Holland, 1976.

[50] F. J. A. Artacho and J. Borwein, "Global convergence of a non-convex Douglas-Rachford iteration," *J. Global Optimizat.*, to be published.

[51] D. L. Donoho and J. M. Johnstone, "Ideal spatial adaptation by wavelet shrinkage," *Biometrika*, vol. 81, no. 3, pp. 425–455, 1994.

[52] J. Fessler, Image reconstruction toolbox 2012, Univ. Michigan [Online]. Available: http://www.eecs.umich.edu/~fessler/code/index.html

[53] E. Meyer, R. Raupach, M. Lell, B. Schmidt, and M. Kachelrie, "Normalized metal artifact reduction (NMAR) in computed tomography," *Med. Phys.*, vol. 37, pp. 5482–5493, 2010.

[54] G. Poludniowski, G. Landry, F. DeBlois, P. M. Evans, and F. Verhaegen, "SpekCalc: A program to calculate photon spectra from tungsten anode X-ray tubes," *Phys. Med. Biol.*, vol. 54, no. 19, pp. N433–N438, 2009.

[55] M. J. Berger and J. H. Hubbell, "XCOM: Photon cross sections on a personal computer," 1987, Center Radiat. Res., Nat. Bureau Standards.

[56] B. Kratz, S. Ens, J. Muller, and T. M. Buzug, "Reference-free ground truth metric for metal artifact evaluation in CT images," *Med. Phys.*, vol. 38, no. 7, pp. 4321–4328, 2011.

[57] J. W. Hoppin, M. A. Kupinski, G. A. Kastis, E. Clarkson, and H. H. Barrett, "Objective comparison of quantitative imaging modalities without the use of a gold standard," *IEEE Trans. Med. Imag.*, vol. 21, no. 5, pp. 441–449, May 2002.

[58] M. Abdoli, M. R. Ay, A. Ahmadian, R. Dierckx, and H. Zaidi, "Reduction of dental filling metallic artefacts in CT-based attenuation correction of PET data using weighted virtual sinograms optimized by a genetic algorithm," *Med. Phys.*, vol. 37, pp. 6166–6177, 2010.

[59] S. Karimi, P. Cosman, C. Wald, and H. Martz, "Segmentation of artifacts and anatomy in CT metal artifact reduction," *Med. Phys.*, vol. 39, no. 10, pp. 5857–5868, 2012.

[60] M. Bal and L. Spies, "Metal artifact reduction in CT using tissue-class modeling and adaptive prefiltering," *Med. Phys.*, vol. 33, no. 8, pp. 2852–2859, 2006.

[61] M. J. Fadili, J.-L. Starck, and F. Murtagh, "Inpainting and zooming using sparse representations," *Comput. J.*, vol. 52, no. 1, pp. 64–79, 2009.